

# Constraints on Midmantle Discontinuities in Mars from Analysis of InSight Seismic Data



Cecilia Durán<sup>\*1</sup>, Amir Khan<sup>\*1,2</sup>, George Helffrich<sup>3</sup>, and Domenico Giardini<sup>1</sup>

## Abstract

The structure and nature of Earth's transition zone, which is delineated by the transformation of olivine to its higher-pressure polymorphs, exerts a strong influence on material transfer between upper and lower mantle. Mars, however, because of its relatively large core, is only expected to exhibit the equivalent of Earth's uppermost transition zone seismic discontinuity. We searched the InSight seismic data for marsquakes and impacts located in an epicentral distance range favorable for detection of seismic phases that have interacted with Mars's olivine transition (midmantle) discontinuity. Through application of careful data selection criteria and processing schemes, we found 13 events in the distance range in which body waves are expected to refract through the midmantle of Mars. Although triplicated body waves are potentially present in seven events, the distance distribution is insufficient to allow for unambiguous detection of the triplicated waveform pattern associated with the midmantle discontinuity. Comparison of travel times of the observed waveforms with predictions from recent Mars models indicates the possible presence of a midmantle discontinuity located between 987 and 1052 km or 1075 and 1122 km depth, in which the uncertainty comes from our inability to reliably distinguish first from secondary arrivals.

**Cite this article as** Durán, C., A. Khan, G. Helffrich, and D. Giardini (2025). Constraints on Midmantle Discontinuities in Mars from Analysis of InSight Seismic Data, *The Seismic Record*, 5(2), 207–217, doi: 10.1785/0320240047.

## Supplemental Material

## Introduction

Throughout the 1440 Sols (a Sol is a Martian day and corresponds to ~24 hr 40 min) that the InSight mission was active on the surface of Mars, more than 2700 seismic events, including marsquakes and meteorite impacts, were detected and cataloged (Ceylan *et al.*, 2022; InSight Marsquake Service, 2023). Despite significant improvement in our knowledge of Mars' interior structure, including observations of intracrustal layering, Moho, a thick lithosphere, a mantle that appears to be equivalent to Earth's upper mantle from a mineralogical point of view, and an entirely liquid core that makes up about 50% of its radius, there are fewer constraints on the structure of the mid-to-lower mantle (depth range ~1000–1700 km) (e.g., Drilleau *et al.*, 2022; Durán, Khan, Ceylan, Charalambous, *et al.*, 2022; Durán, Khan, Ceylan, Zenhäusern, *et al.*, 2022; Lognonné *et al.*, 2023). This is in part due to the geographical distribution of the low-magnitude seismic events ( $M_w \sim 2.5$ –4.6) with generally poor signal-to-noise ratio (Ceylan *et al.*, 2023; Kawamura *et al.*, 2023) that

have been recorded and in part because of intense near-receiver scattering presenting observational challenges to detecting seismic phases that have traversed Mars' mid-to-lower mantle (Durán *et al.*, 2022).

Of importance about mantle structure is the depth to and sharpness of Mars' olivine transition seismic discontinuities (MOTDs). On Earth, these result from the transformation of olivine to its higher-pressure polymorphs, wadsleyite, and ringwoodite, at depths of about 410 and 660 km, respectively, that bound the mantle transition zone (e.g., Helffrich, 2000).

1. Institute of Geophysics, ETH Zurich, Zurich, Switzerland, <https://orcid.org/0000-0003-4269-930X> (CD); <https://orcid.org/0000-0002-7787-4836> (AK); <https://orcid.org/0000-0002-5573-7638> (DG);
2. Institute of Geochemistry and Petrology, ETH Zurich, Zurich, Switzerland;
3. ELSI, Institute of Science Tokyo, Tokyo, Japan, <https://orcid.org/0000-0002-7363-4552> (GH)

\*Corresponding authors: cecilia.duran@eaps.ethz.ch; amir.khan@eaps.ethz.ch

© 2025. The Authors. This is an open access article distributed under the terms of the CC-BY license, which permits unrestricted use, distribution, and reproduction in any medium, provided the original work is properly cited.

Because of the Mars' smaller size and its relatively large core, however, only the discontinuity associated with the transformation of olivine, which occurs somewhere between 12 and 14 GPa, corresponding to depths of 1000–1200 km, is expected to be observed, as illustrated in Figure S1, available in the supplemental material to this article. Given the pressure, temperature, and compositional dependence of this mineral transformation, imaging an MOTD holds the potential of providing insights into the thermochemical structure of the mantle. The depth, and hence pressure, at which the discontinuity could be observed would give a temperature constraint at that depth because it is primarily influenced by mantle temperature (Munch *et al.*, 2018), although composition may have a greater effect on the depth of this transition at higher temperatures (Khan, Liebske, *et al.*, 2021). Projecting that temperature upward and downward to the boundaries of the mantle, the base of the lithosphere and the core-mantle boundary, would provide important geophysical constraints on for example, the style of convection in Mars (Cheng *et al.*, 2024; Murphy and King, 2024), the absence of a present-day magnetic field (Mittelholz *et al.*, 2020), and the flexure of Mars's lithosphere (Broquet *et al.*, 2020).

Seismic phases sensitive to midmantle structure include body-wave conversions at, triplications from, and underside reflections off the MOTDs. Huang *et al.* (2022) recently reported on the seismic detection of a Martian MOTD at a depth of about 1000 km through analysis of triplicated waveforms. Moreover, Deng and Levander (2023), using single-station autocorrelation analysis, reported observation of a reflection response that was interpreted to emanate from the Martian olivine–wadsleyite transition. However, where Huang *et al.* (2022) only had five teleseismic events at their disposal, there are now 13 events available at the appropriate epicentral distance range for detecting seismic phases that have interacted with MOTDs. Building on the earlier results and given the larger number of events at our disposal, we report on a complete analysis of the InSight event data that have *P*- and *S*-wave turning points between ~1000 and 1200 km depth and, as a consequence, have spent part of their trajectory in the MOTD. Following this, we realign, relocate, and subsequently determine more precise event back azimuths in an attempt to improve the detection of MOTD-interacting phases. Finally, we compare the observed data with predictions based on the most up-to-date models of Mars' interior structure and attempt to infer the characteristics of the Martian MOTD based on the available evidence presented here.

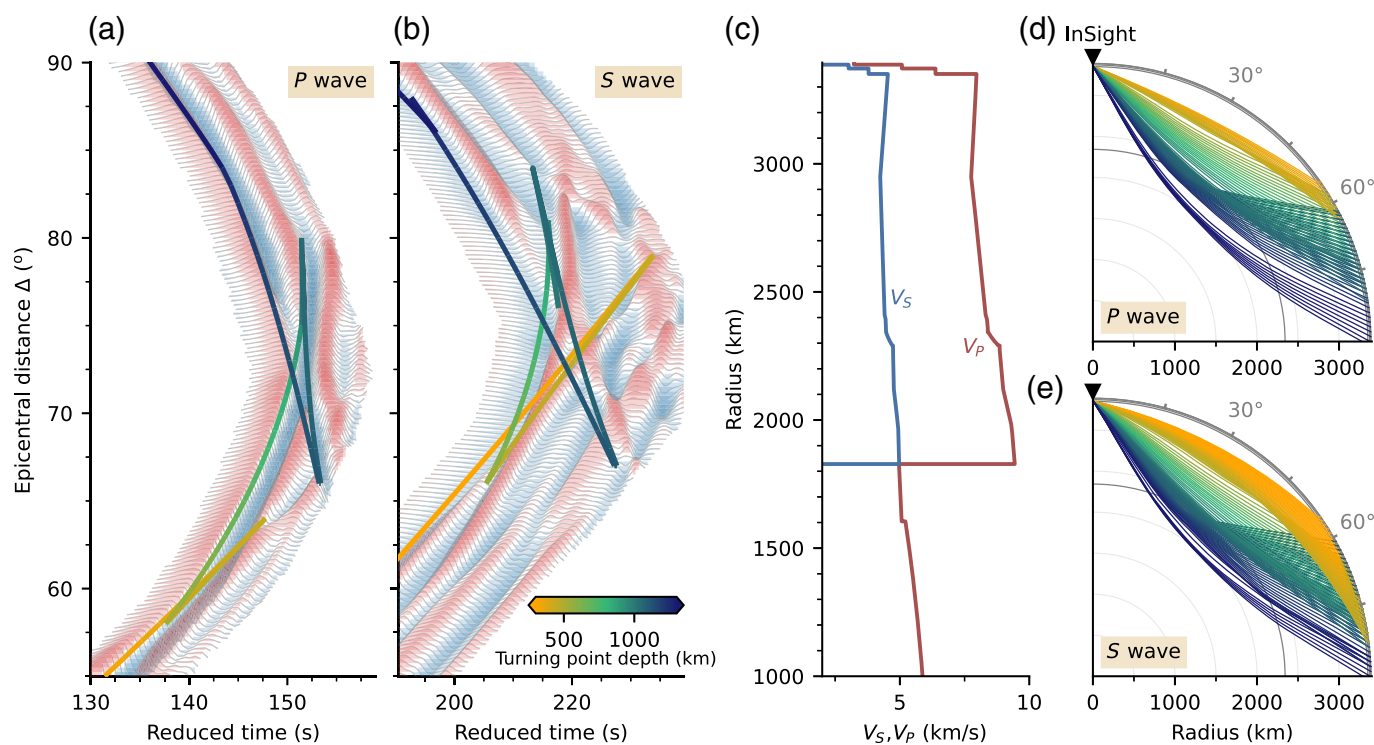
## Triplicated Body Waves

As a result of the increase in seismic wave velocities associated with a Martian MOTD, three arrivals corresponding to direct, reflected, and refracted *P* and *S* waves are predicted to be observed within a short time window at distances between ~65° and 85°. This phenomenon is referred to as “triplication” and is illustrated in Figure 1 based on synthetic *P*- and *S*-waveform sections and ray paths for a representative Martian seismic velocity model. The Mars models used herein are based on a joint geophysical–mineral physics parameterization (e.g., Khan, Ceylan, *et al.*, 2021; Durán *et al.*, 2022) that incorporates the olivine transition and are obtained from the most up-to-date differential body-wave travel time and astronomic–geodetic data set (Khan *et al.*, 2023) (see [Data and Resources](#) for model availability). The high-frequency (HF) (1 Hz) waveforms were computed using AxiSEM by Nissen-Meyer *et al.* (2014) for a source located at 40 km depth and dominated by normal faulting (Jacob *et al.*, 2022). Although this source may not represent the focal mechanism of events outside of Cerberus Fossae, which is the most seismically active region seen by InSight (Stähler *et al.*, 2022), it serves to capture the main characteristics of Martian triplicated waves.

More generally, detection of separate triplicated waveform branches, as illustrated in Figure 1, depends not only on the velocity structure but also on the duration of the source time function and the frequency range under consideration (e.g., Bissig *et al.*, 2022). Triplicated *S* waves exhibit longer differential travel times than *P* waves because *S* waves travel at slower velocities than *P* waves. Consequently, where triplicated *P* waves are expected to arrive within ~10 s of the first arrival, the time window for triplicated *S* waves increases to ~20 s after the main *S*-wave arrival. Figure 1 also shows that where *P* waves exhibit a well-defined triplicated waveform pattern, amplitudes of triplicated *S* waves potentially suffer from interference of other seismic phases, including the depth phases and associated triplications. Finally for the Martian model considered here, interference arises from negative upper mantle *S*-wave velocity gradients, which act to produce an additional late triplicated branch (yellow ray paths in Fig. 1d,e), corresponding to shallow propagation.

## InSight Seismic Data

The Marsquake Service (MQS) has classified all seismic events recorded by InSight according to frequency content as either low-frequency (LF), HF, or wideband (WB) events (Ceylan *et al.*, 2022). The LF family comprises events with energy



mainly below 1 Hz and mostly clear *P*- and *S*-wave arrivals with an overall duration of ~10–30 min. The HF family consists of events with predominant energy above 1 Hz (up to ~12 Hz) and with a duration ranging from 5 to 20 min. The WB events, on the other hand, include events with energy spanning from well below 1 Hz to well above 4 Hz. The WB class also includes some events previously classified as LF, for example, the imaged meteoroid impacts (Posiolova *et al.*, 2022) and the largest event detected during the mission (Kawamura *et al.*, 2023), but also marsquakes previously grouped into the HF family that were considered to be trapped waves propagating in the Martian crust (van Driel *et al.*, 2021).

Of importance in the analysis of Martian seismic data is removal of nonseismic signals related to atmospheric perturbations, transient signals (e.g., glitches), lander reverberations, subsurface resonances, and instrument artifacts (Ceylan *et al.*, 2021). To limit their impact, MQS have produced a complete catalog of denoised event waveforms through application of deep learning models (see Dahmen *et al.*, 2024 for details).

### Initial data processing and phase refinement

Events are labeled by the InSight team by mission Sol of occurrence and sub-labeled alphabetically for Sols with more than one event. The events considered here and by Huang *et al.* (2022), including MQS epicentral distance estimations and

**Figure 1.** Synthetic *P*- and *S*-waveform sections. (a) *P*-waveform (vertical component) and (b) *S*-waveform (transverse component) sections for a range of epicentral distances showing triplicated waveforms. The blue-green “bow-tie” branches in panels (a) and (b) outline a classic discontinuity triplication, whereas the yellow branches correspond to the end of a shadow zone caused by the *P*- and *S*-wave low-velocity zones. *P* and *S* waveforms are band-pass filtered in the ranges 1–10 s and 2–20 s, respectively, and aligned using reduced velocities of 12 and 6 km/s, respectively. Travel-time curves are color coded according to bottoming depth. (c) Representative Martian seismic velocity model taken from the most recent model collection of Khan *et al.* (2023). (d,e) Ray paths taken by the direct, reflected, and refracted *P* and *S* waves through the Martian mantle. The source is located at 40 km depth and assumes a normal-faulting focal mechanism, representative of marsquakes originating in Cerberus Fossae. Waveforms were computed using AxisEM (Nissen-Meyer *et al.*, 2014).

quality labels (InSight Marsquake Service, 2023) are summarized in Table 1. Of these, only two events are quality A, characterized by high signal-to-noise ratio (SNR), clearly distinguishable *P*- and *S*-wave arrivals, and determinable back azimuths. The remaining events are quality B and C, with lower SNR and partly indistinct phase arrivals. Of the five events analyzed by Huang *et al.* (2022), we excluded S0345a (quality C), partly because of unclear phase arrivals and partly because its waveform envelopes are similar to those of more distant events (Ceylan *et al.*, 2023). Significant deviations also

Table 1

## List of Events that Potentially Sample the Midmantle Structure of Mars

Event	MQS Determination		Refined Phases and Back Azimuths			
	Quality	Distance (°)	$T_P$ (UTC) $\pm$ Uncertainty (s) (yyyy/mm/dd hh:mm:ss)	$T_S \pm$ Uncertainty (s)	Back Azimuth (°)	BAZ Quality
S0167b	C	n.d.	2019/05/17 19:31:34 $\pm$ 3	415.8 $\pm$ 2	124.5	R
S0185a*	B	60.9 $\pm$ 8.4	2019/06/05 02:14:08 $\pm$ 3	344.5 $\pm$ 12 (360.4 $\pm$ 7.5)	156.4 (161 $\pm$ 8.2)	U
S0234c*	C	n.d.	2019/07/25 12:54:33 $\pm$ 10	329.6 $\pm$ 2 (394.9 $\pm$ 10)	116.4 (258.5 $\pm$ 72.1)	R
S0264e	B	69.3 $\pm$ 4.6	2019/08/25 10:31:46 $\pm$ 2	335.0 $\pm$ 4	340.0	U
S0345a*	C	n.d.	—	—(373.6 $\pm$ 10)	—(179 $\pm$ 12.1)	—
S0421a	B	69.3 $\pm$ 7.2	2020/02/02 17:38:09 $\pm$ 4	414.8 $\pm$ 3	357.3	R
S0424c	B	55.1 $\pm$ 4.5	2020/02/05 17:30:04 $\pm$ 9	324.0 $\pm$ 6	185.5	U
S0923d	C	91.8 $\pm$ 15.3	2021/07/02 12:16:25 $\pm$ 10	492.2 $\pm$ 2	44.5	R
S1094b*	A	60.3 $\pm$ 3.6	2021/12/24 22:45:07 $\pm$ 4	347.2 $\pm$ 3 (358.4 $\pm$ 5)	51.4 (35.9 $\pm$ 6.5) <sup>§</sup>	R
S1102a*	A	73.3 $\pm$ 4.5	2022/01/02 04:35:30 $\pm$ 3	407.6 $\pm$ 3 (410.2 $\pm$ 10)	270.0 (92 $\pm$ 42.2)	R
S1153a	B	84.8 $\pm$ 10.5	2022/02/23 21:09:50 $\pm$ 4	458.0 $\pm$ 2	87.3	R
S1157b <sup>†</sup>	C	n.d.	2022/02/27 02:39:12 $\pm$ 60	443.7 $\pm$ 2	—	—
S1237a <sup>††</sup>	C	91.1 $\pm$ 16.0	2022/05/20 23:14:09 $\pm$ 20	413.7 $\pm$ 60	—	—
S1415a	B	88.2 $\pm$ 9.6	2022/11/19 21:56:33 $\pm$ 3	448.2 $\pm$ 4	262.7	U

Refined absolute  $P$ -wave arrival-time picks,  $S$ -wave differential travel times (relative to  $P$ ), and estimated back azimuth based on polarization and particle motion analysis from this study. The “BAZ Quality” label refers to reliability of the back-azimuth estimates obtained here, in which R is reliable and U is unreliable. Entries marked “—” indicate that the particular event has been removed from consideration. Numbers in parentheses indicate the  $S$ – $P$  differential travel time and back-azimuth determinations of Huang *et al.* (2022). Quality labels and epicentral distances determined by the Marsquake Service (MQS) (InSight Marsquake Service, 2023) are listed for comparison. n.d. indicates that epicentral distance could not be determined by MQS.

\*Events considered by Huang *et al.* (2022).

<sup>†</sup> $P$ -wave arrival could not be refined relative to MQS.

<sup>††</sup> $S$ -wave arrival could not be refined relative to MQS.

<sup>§</sup>Back-azimuth estimation derived from orbital images of impact.

exist for S0234c (quality C). Where we find an  $S$ – $P$  differential travel time of 329.6 s based on the denoised data, Huang *et al.* (2022) uses 395 s; yet, the  $P$  wave is unobservable in the “original” data. In addition, for impact event S1094b, Huang *et al.* (2022) used a back azimuth of  $35.9^\circ \pm 6.5^\circ$  in place of  $51.4^\circ$  derived from orbital images of the impact (Posiolova *et al.*, 2022). The WB class events, meanwhile, are characterized by relatively large uncertainties in arrival times and therefore in epicentral distances. Thus, initial refinement of the main  $P$ - and  $S$ -wave arrivals is required prior to searching for triplicated phases.

For this, we follow Durán *et al.* (2022) and use raw and polarized waveforms and equivalent time-domain envelopes, in addition to three-component scalograms to enhance

body-wave arrivals in the low magnitude, noisy marsquake signals. The procedure is illustrated for WB event S1153a in Figure 2. Equivalent figures of denoised and nondenoised waveforms for all 13 events considered here are shown in Figures S2–S13. Although denoised waveforms seemingly provide clearer phase arrivals, the removal of important signal has been noticed in some cases. Consequently, we simultaneously analyze both denoised and nondenoised waveforms throughout. The scalogram indicates the arrival of energy from well below 0.1 to 1 Hz and above.

A zoom into the band-pass-filtered denoised waveforms and their time-domain envelopes are shown in Figure 2 (Panel I) for time windows containing the  $P$ - and  $S$ -wave arrivals, respectively. To increase the SNR of body waves, we follow

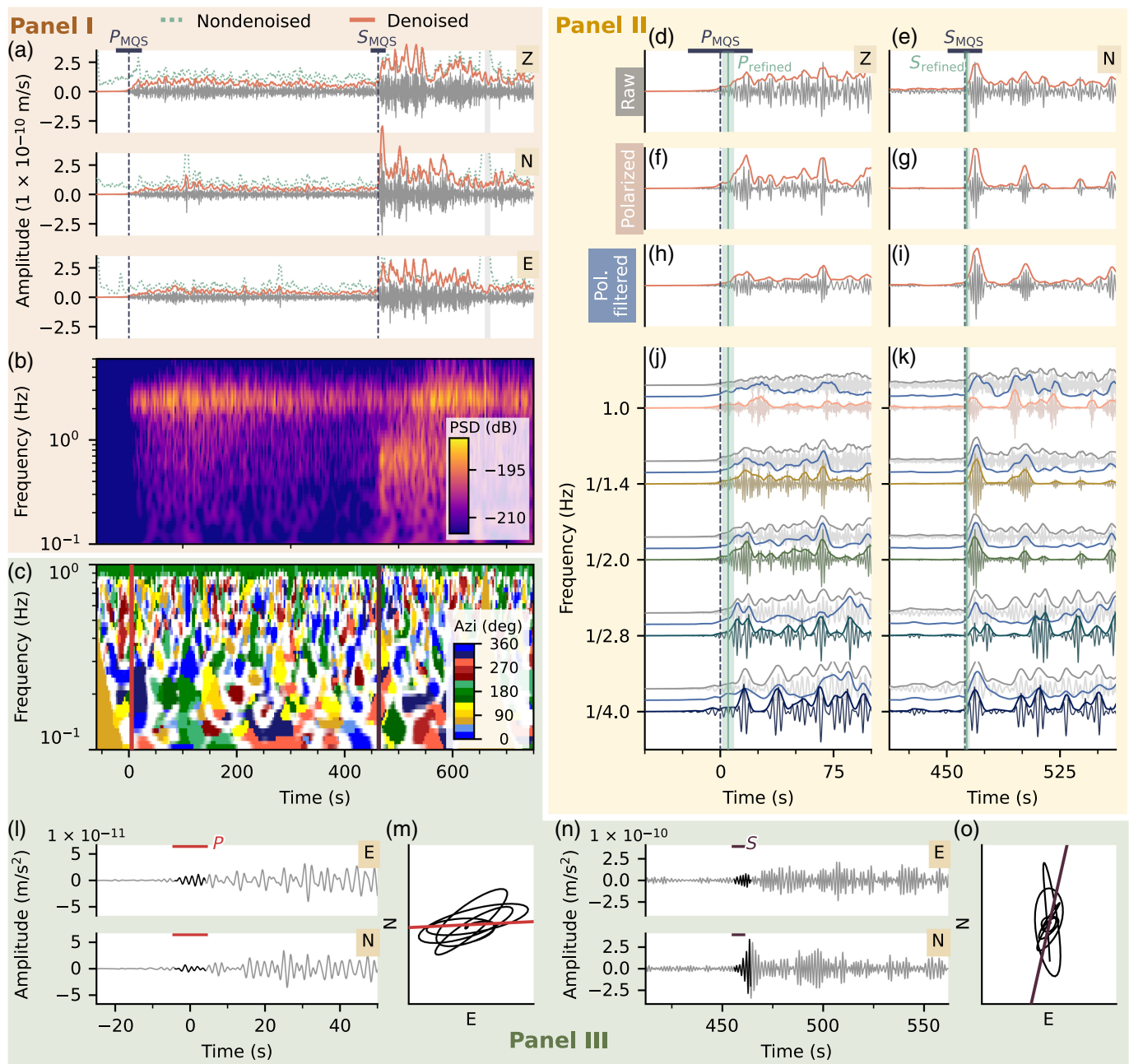


**Figure 2.** Overview of event analysis illustrated for event S1153a. Initial data processing (Panel I), body-wave refinement (Panel II), and polarization analysis for back-azimuth determination (Panel III). In Panel I are shown denoised (Dahmen et al., 2024) band-pass filtered (0.2–0.8 Hz) waveforms and their time-domain envelopes, including nondenoised envelopes, for the vertical, north, and east components (a), together with a three-component scalogram for the denoised data set (b). Panel II shows band-pass-filtered raw (d,e) and polarized waveforms (f,g), and band-pass-filtered waveforms after the application of polarization analysis (Pol. filtered) (h,i). Raw (gray), Polarized (colored), and Pol. filtered (blue) waveforms and time-domain envelopes across different frequency bands (filter banks) are shown in (j) and (k). *P*- and *S*-wave arrival-time

picks and uncertainties by InSight Marsquake Service (2023) are represented by dashed gray lines and horizontal black bars at the top of Panel II, respectively. *P*- and *S*-wave arrival-time picks and uncertainties made in this study are represented by green solid lines and bars, respectively. Panel III shows back-azimuth analysis, including azimuthal directions as a function of time and frequency (c) and horizontal particle motion analysis for the *P* wave (l,m) and the *S*-wave (n,o). (c) Azimuths of around  $0^\circ$  for the low-frequency (0.3–0.7 Hz, blue patch) *P*-wave arrival and around  $90^\circ$  for the *S*-wave arrival (0.5–0.9 Hz, yellow patch) are found. Hodograms in (m) and (o) are compared with the direction of motion estimated from (c) as described in Zenhäusern et al. (2022). Similar overviews are available for all events considered in this study (see Figs. S2–S13).

Durán *et al.* (2022) and apply a time-domain polarization filter that exploits the linear polarization characteristic of body waves. Through principal-component analysis, this method enhances the linearly polarized components in the signal as indicated in the filtered polarized vertical (Z) and horizontal (N) component waveforms for event S1153a. Because *P*- and *S*-wave arrivals are distinguished not only by their strong linear polarization, but also by their near-vertical and near-horizontal inclinations (for a close-to-vertical incidence angle), respectively, we also perform a three-component polarization analysis and use TwistPy (see [Data and Resources](#)) to filter in the time–frequency domain. This filtering workflow effectively identifies and suppresses (or preserves) features in the waveforms by making use of the polarization attributes of the signal and has been applied to remove glitches (Durán *et al.*, 2024) and enhance body waves (Brinkman *et al.*, 2023). To further strengthen body-wave arrivals, we apply a filter mask that preserves signals with ellipticity values below 0.5 and inclinations between 0° and 30° for *P* waves and 60° and 90° for *S* waves, measured from vertical. The polarized and polarization-filtered (after application of TwistPy) waveforms exhibit a series of high-amplitude packages of energy associated with body waves.

A complementary method for identifying seismic phases involves the use of narrow-band-filtered time-domain waveforms and their envelopes, labeled filter banks (e.g., Khan, Ceylan, *et al.*, 2021; Durán *et al.*, 2022). To this end, we filter the velocity traces in frequency bands half an octave wide, centered on frequencies ranging from 1/4 to 1 Hz, which captures the signal's LF energy. Waveform filter banks and time-domain envelopes, along with raw, polarized, and polarization-filtered waveforms (only envelopes are displayed for the latter) are shown in Figure 2 (Panel II) for the denoised data set. The onset of energy associated with both *P*- and *S*-wave arrivals is apparent in the envelopes across most frequencies and in the raw, polarized, and polarization-filtered waveforms.

For a phase to be identified as a body-wave arrival, it must conform to the following set of criteria: (1) be present across different frequency bands; (2) be present in both, raw and polarized traces/envelopes; and (3) differential travel time between phase pairs follows a sequence for example,  $PPP - PP < PP - P$ . In addition to these criteria, we also require that body-wave arrivals must be consistent in both denoised and nondenoised waveforms, as well as in the polarization-filtered waveforms. Following these criteria, we selected the *P*- and *S*-wave arrivals indicated by vertical green lines in Figure 2 (Panel II), whereas arrival-time uncertainties are represented

by green bars. A similar analysis has been applied to all events (see Figs. S2–S13).

### Polarization analysis for azimuth determination

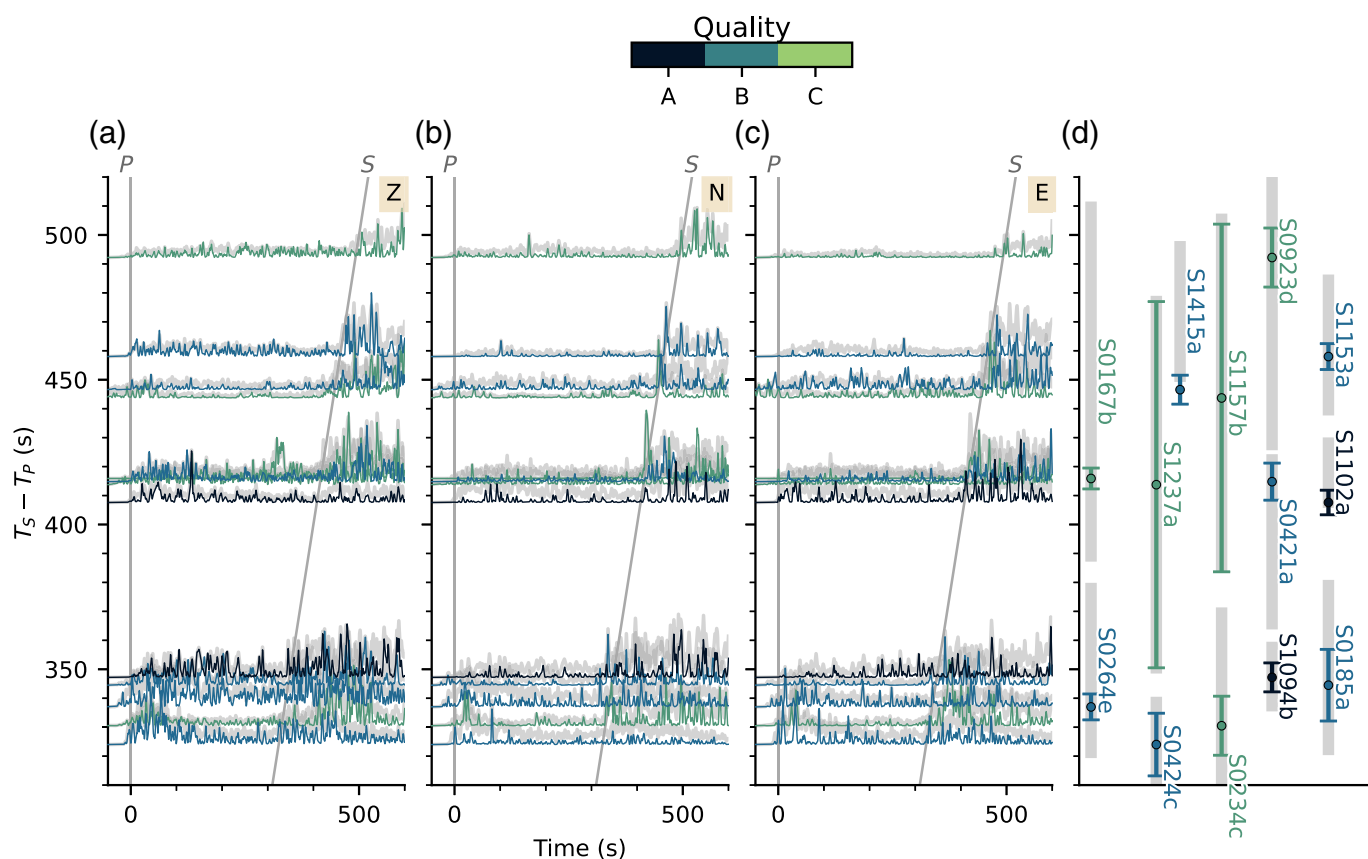
Tripllicated *S*-wave identification typically relies on transverse (T)-component waveforms, which require estimating the back azimuth. For this, we use particle-motion estimates from time–frequency polarization analysis and hodograms based on the work of Zenhäusern *et al.* (2022). The time–frequency polarization analysis relies on transforming the data into the time–frequency domain using continuous wavelet transformation and then performing eigen-analysis on the resulting spectral matrix. The instantaneous back azimuth is determined by projecting the semimajor axis of the best-fitting polarization ellipse onto the horizontal plane. Because this axis is more stable for rectilinear signals, it provides a reliable constraint for *P*- and *S*-wave arrivals.

The estimated azimuth as a function of time and frequency for the entire waveform is shown in Figure 2c (Panel III). To determine azimuth based on *P* and *S* waves, we computed azimuthal probability densities for the time windows centered on the *P*- and *S*-wave arrival picks, widths for which are determined by the assigned arrival-time uncertainty, for frequencies ranging between 0.3 and 0.7 Hz and 0.5 and 0.9 Hz, respectively. The maximum of the *P*-wave azimuthal probability density curve (not shown for brevity) is considered representative of the back azimuth of the event, whereas the *S* wave is used for corroboration (see Zenhäusern *et al.*, 2022 for details). The so-obtained back azimuths are indicated in Figure 2m,o (Panel III, orange solid and black line).

To validate the azimuths, we compute *P*- and *S*-wave horizontal particle motion hodograms, using the same time and frequency range as in the polarization analysis. The filtered waveforms, centered on the main body-wave arrivals, along with the corresponding hodograms, are displayed in Figure 2m–o (Panel III) and are seen to align with the direction determined from the time–frequency polarization analysis. Similar polarization analysis is conducted for all events (see Figs. S2–S13). Table 1 summarizes estimated back azimuths for all events. To each event, we have also assigned a quality label based on the reliability of the estimated back azimuth. For comparison, MQS only determined the back azimuth for S1102a.

### Realignment

Our final set of body-wave picks and corresponding uncertainties of *P*- and *S*-wave arrivals for the 13 events considered in



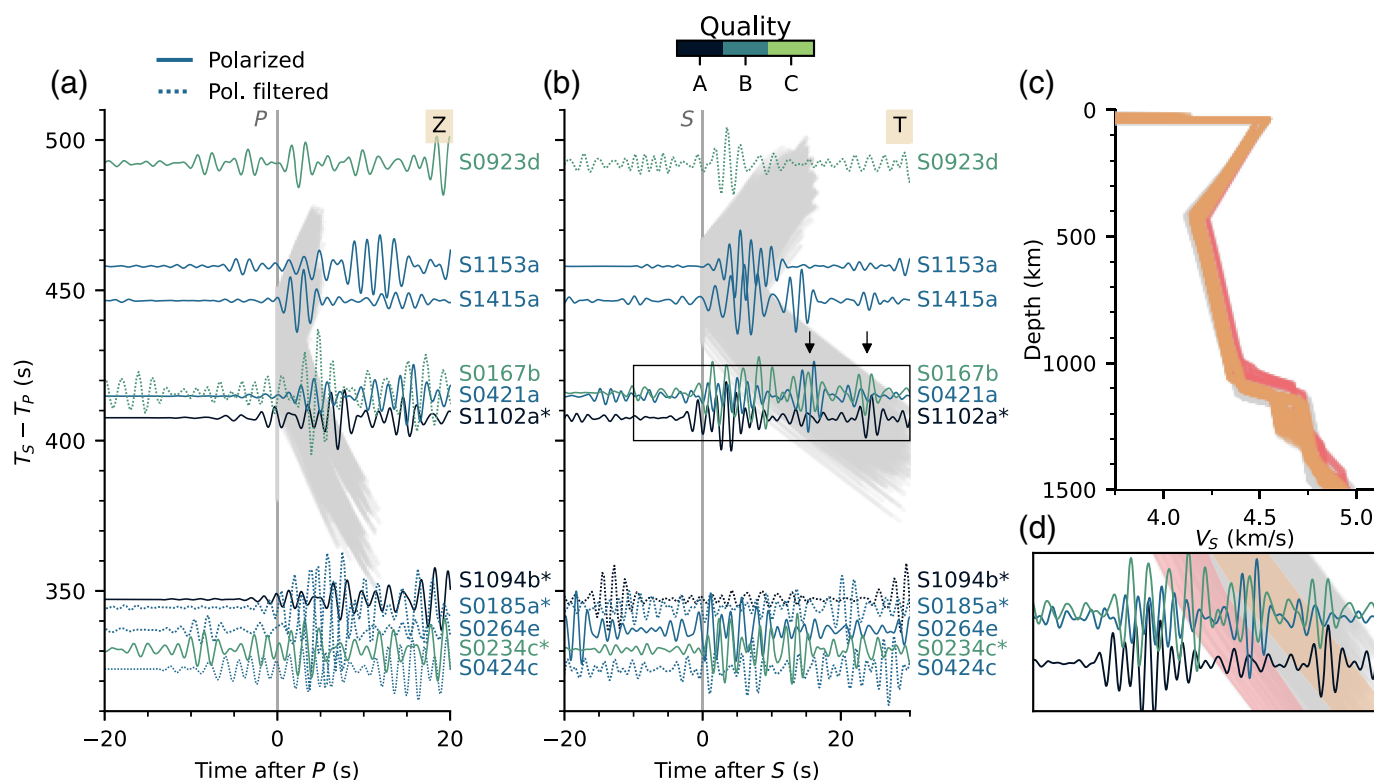
this study are listed in Table 1, whereas the realigned envelopes, along with their updated differential travel-time uncertainties, are summarized in Figure 3. Although uncertainty in differential  $S-P$  time, which is a proxy for epicentral distance, is significantly reduced for most body waves compared to those of MQS, some, particularly the weaker low-frequency  $P$  waves (e.g., S1237a and S1157b), do not meet our criteria and are, therefore, discarded from further analysis.

## Results and Discussion

Polarized and polarization-filtered  $P$ - and  $S$ -waveform sections rotated into the ZRT system are shown in Figure 4, with only the clearest of the two shown to avoid clutter. For comparison, predicted  $P$ - and  $S$ -wave travel times based on the most up-to-date Mars models from Khan *et al.* (2023) are also shown (see Data and Resources). The comparison allows several observations to be made. First, phase refinement in the absence of the denoised data would not have been possible. Second, of the 13 events considered, we focus on the 7 events that cover the appropriate epicentral distance range ( $S-P$  differential travel time of  $\sim 360$ – $490$  s), in which triplicated phases are expected. Third, in spite of careful data selection and processing,

**Figure 3.** Overview of realigned broadband events within the travel time range in which triplications are expected. (a–c) Time-domain envelopes of vertical- (Z), north- (N), and east-component (E) band-pass filtered (0.2–0.8 Hz) denoised (Dahmen *et al.*, 2024) polarized waveforms are shown and color coded according to their quality (A–C) (InSight Marsquake Service, 2023). Nonpolarized time-domain envelopes are displayed in gray. (d) Comparison between  $S-P$  differential travel times determined by the Marsquake Service (gray vertical bars) and this study (colored circles and error bars). Time is relative to the refined arrival of the  $P$  wave (see Table 1).

waveforms remain noisy. This is not unexpected in view of the fact that most events are either quality B or C. Fourth, with a noncontinuous epicentral distance coverage, observing the characteristic triplicated waveform pattern (compare with Fig. 1) is challenging. Fifth, uncertainties in  $S-P$  differential travel time (see Table 1) average about  $\pm 5$  s, implying that individual events can be considered reasonably well located in distance, but not necessarily in direction (uncertainties associated with back-azimuth determination of quality B and C events is significant). This implies that the rotation into the ZRT system is possibly only approximate, as a result of which the sought-after seismic phases are potentially present on multiple



components. Finally, because individual arrivals occur within  $\sim 10$  and  $20$  s of the main  $P$  and  $S$  waves, respectively, and most mantle-traversing body waves are detected at frequencies between  $0.2$  and  $0.8$  Hz, resolution is generally insufficient, particularly in the case of  $P$  waves, to distinguish first from secondary arrivals. In the case of event S1102a (quality A), for example, the main  $P$  wave, the depth phase, and the triplicated  $P$  waves are expected to arrive within just a few seconds of each other, making identification of either of these challenging. Nonetheless, a number of repeating wave packets are present in the transverse-component waveforms. For the three events that group together toward the lower triplication branch, S1102a–S0421a–S0167b, two recurring wave packets, indicated by arrows in Figure 4, are seen in the waveforms and at about the same relative location. For S1415a–S1153a, toward the middle of the triplication, a single recurring wave packet is observed. On account of the recurrence, the indicated wavepackets are unlikely to be related to random noise and can therefore be employed for model down-selection. This is illustrated in Figure 4, in which the predicted travel time ranges based on the models of Khan *et al.* (2023) (gray lines) have been sorted according to overlap with the two wavepackets seen in the seismograms of events S1102a–S0421a–S0167b. The corresponding models are also shown in Figure 4 and indicate

**Figure 4.**  $P$ - and  $S$ -waveform sections from events that possibly interacted with midmantle discontinuities in Mars. (a) Vertical-component  $P$ -waveform section showing potentially triplicated  $P$  waves; (b) transverse-component  $S$ -waveform section showing potentially triplicated  $S$  waves. Superimposed (gray) are predicted  $P$ - and  $S$ -wave travel times based on the most recent Martian interior structure models of Khan *et al.* (2023). Arrows indicate the arrival of two potential triplicated phases. (c)  $S$ -wave velocity profiles color coded according to which models fit the first (in red) and the second (in yellow) of the two potential arrivals as indicated in the zoom-in in panel (d). Observed  $P$  and  $S$  waveforms in panels (a) and (b) represent either polarized or polarization-filtered waveforms, depending on which is least noisy. Observed waveforms are filtered between  $0.4$  and  $0.8$  Hz. The differential  $S$ – $P$  travel time is a proxy for epicentral distance. Event labels are indicated on the right side in panels (a) and (b) and events marked with "\*" designate those considered by Huang *et al.* (2022).

MOTD depths in the ranges  $987$ – $1052$  km (red models matching travel time of first wavepacket) and  $1075$ – $1122$  km (yellow models matching travel time of second wavepacket) (see inset in Fig. 4), respectively. Events S1415a–S1153a provide little additional information as these appear to be sitting in the center of the triplication, which is compatible with the observation of a single large wavepacket.

Incidentally, our shallower depth range is compatible with the results from Huang *et al.* (2022), who found a midmantle

discontinuity at a depth of  $1006 \pm 40$  km using a waveform matching approach. Although the latter potentially represents a more quantitative means of assessing the depth of the mid-mantle discontinuity, the study of [Huang \*et al.\* \(2022\)](#) nevertheless relied on several assumptions, including known source mechanisms and separate fitting of *P* and *S* waveforms using distinct thermochemical models, which showed that a singular model among the structures that fit both types of data could not be isolated. [Deng and Levander \(2023\)](#) interpreted a peak in the noise autocorrelation at a lag of  $\sim 280$ – $285$  s to be associated with the olivine transition and, using premission seismic velocity models of Mars, estimated its depth to range between 1110 and 1170 km. Converting their time lag using an average velocity model created from the [Khan \*et al.\* \(2023\)](#) model database (see [Data and Resources](#)) corresponds to a depth range of  $1071 \pm 5$  km (280 s) and  $1092 \pm 5$  km (285 s), which is compatible with the deeper range found here but incompatible with that of [Huang \*et al.\* \(2022\)](#).

Thus, although evidence for a midmantle seismic discontinuity continues to be strengthened, the uncertainties on the location of the Martian MOTD at present are such that any thermochemical inferences made from the mapped MOTD depths must be considered provisional. A joint approach incorporating noise autocorrelation analysis, however, may be a viable way forward to improve upon current estimates of MOTD depth.

## Conclusion

We reanalyzed the entire InSight seismic data set for marsquakes and impacts that have interacted with the Martian mid-mantle seismic discontinuity associated with the olivine transition, which is predicted to occur in the midmantle of Mars. The depth of this discontinuity is desirable because it anchors the thermochemical structure of Mars's mantle. Our search resulted in seven events at the required epicentral distance from the InSight station. Based on matching differential travel times of triplicated body-wave phases, we find tentative evidence for a seismic discontinuity in either of the depth ranges 987–1052 km or 1075–1122 km, in line with results obtained from two earlier studies. The uncertainty reflects our current inability to properly separate the different body-wave phases in the observed waveforms. This is related to the limited number of useful events and their generally poor SNR (most of the available events are quality B and C). With only half of the considered events located at epicentral distances where interaction with a midmantle discontinuity is expected, the poor epicentral

distance distribution of the events makes identification of the waveform pattern characteristic of triplications challenging. A combination of different data sets may help resolve this impasse. To seismically image the Martian midmantle structure in more detail in future missions will require a significantly improved SNR, which can be achieved through proper shielding of the seismometer(s) and solid grounding on bedrock. On account of the low seismicity of the planet, with only a single magnitude-4.6 event recorded in 4 yr, mission longevity will be another important factor.

## Data and Resources

The InSight event catalog V14 (comprising all events until the end of the mission) and waveform data are available from the Incorporated Research Institutions for Seismology Data Management Center (IRIS-DMC), National Aeronautics and Space Administration Planetary Data System (NASA PDS), SEIS-InSight data portal, Institut de Physique du Globe de Paris (IPGP) data center (<https://www.insight.ethz.ch/seismicity/catalog/v14>, last accessed March 2025) and MarsQuake Service catalog by [InSight Marsquake Service \(2023\)](#). The data were processed with ObsPy, NumPy, SciPy, and TwistPy, and visualizations were created with Matplotlib. Synthetic waveforms were computed employing AxiSEM ([Nissen-Meyer \*et al.\*, 2014](#)), and travel-time curves and ray paths employing TauP ([Crotwell \*et al.\*, 1999](#)). The interior Martian structure models from [Khan \*et al.\* \(2023\)](#) that are used in the present analysis are available in digital format from doi: [10.18715/IPGP.2023.llxn7e6d](https://doi.org/10.18715/IPGP.2023.llxn7e6d). Raw and denoised waveform data for the events considered here are available from doi: [10.5281/zenodo.14228799](https://doi.org/10.5281/zenodo.14228799). The TwistPy data are available at <https://twistpy.org/> (last accessed November 2024). The supplemental material includes text and 13 figures, which describe the olivine phase diagram under Martian conditions and data processing, phase refinement and azimuth analysis for all events considered in this study.

## Declaration of Competing Interests

The authors acknowledge that there are no conflicts of interest recorded.

## Acknowledgments

The authors acknowledge National Aeronautics and Space Administration (NASA), CNES, partner agencies and institutions (UKSA, SSO, DLR, JPL, IPGP-CNRS, ETHZ, ICL, MPS-MPG), and the operators of Jet Propulsion Laboratory

(JPL), SISMOC, MSDS, Incorporated Research Institutions for Seismology Data Management Center (IRIS-DMC) and PDS for providing SEED SEIS data. C. D., A. K., and D. G. would like to acknowledge support from ETH through the ETH+ funding scheme (ETH+02 19-1: “Planet Mars”). Part of this research was also supported by the Swiss National Science Foundation through Grant 197369. The authors are grateful to three referees for constructive comments that helped improve the clarity of the article. Finally, the authors would like to thank Keith Koper for efficient editorial handling. This is InSight contribution 350.

## References

- Bissig, F., A. Khan, and D. Giardini (2022). Evidence for basalt enrichment in the mantle transition zone from inversion of triplicated *P*- and *S*-waveforms, *Earth Planet. Sci. Lett.* **580**, 117387, doi: [10.3929/ethz-b-000530943](https://doi.org/10.3929/ethz-b-000530943).
- Brinkman, N., D. Sollberger, C. Schmelzbach, S. C. Stöhler, and J. Robertsson (2023). Applications of time-frequency domain polarization filtering to InSight seismic data, *Earth Space Sci.* **10**, no. 11, e2023EA003169.
- Broquet, A., M. A. Wicczorek, and W. Fa (2020). Flexure of the lithosphere beneath the north polar cap of Mars: Implications for ice composition and heat flow, *Geophys. Res. Lett.* **47**, no. 5, e2019GL086746.
- Ceylan, S., J. F. Clinton, D. Giardini, M. Böse, C. Charalambous, M. van Driel, A. Horleston, T. Kawamura, A. Khan, G. Orhand-Mainsant, *et al.* (2021). Companion guide to the marsquake catalog from InSight, Sols 0–478: Data content and non-seismic events, *Phys. Earth Planet. Int.* **310**, 106597.
- Ceylan, S., J. F. Clinton, D. Giardini, S. C. Stöhler, A. Horleston, T. Kawamura, M. Böse, C. Charalambous, N. L. Dahmen, M. van Driel, *et al.* (2022). The marsquake catalogue from InSight, sols 0–1011, *Phys. Earth Planet. Int.* 106943.
- Ceylan, S., D. Giardini, J. F. Clinton, D. Kim, A. Khan, S. C. Stöhler, G. Zenhäusern, P. Lognonné, and W. B. Banerdt (2023). Mapping the seismicity of Mars with InSight, *J. Geophys. Res. Planets* **128**, no. 8, e2023JE007826.
- Cheng, K. W., A. B. Rozel, G. J. Golabek, H. A. Ballantyne, M. Jutzi, and P. J. Tackley (2024). Mars’s crustal and volcanic structure explained by southern giant impact and resulting mantle depletion, *Geophys. Res. Lett.* **51**, no. 6, e2023GL105910.
- Crotwell, H. P., T. J. Owens, and J. Ritsema (1999). The TauP toolkit: Flexible seismic travel-time and ray-path utilities, *Seismol. Res. Lett.* **70**, no. 2, 154–160.
- Dahmen, N. L., J. F. Clinton, S. C. Stöhler, M.-A. Meier, S. Ceylan, F. Euchner, D. Kim, A. Horleston, C. Durán, G. Zenhäusern, *et al.* (2024). Revisiting Martian seismicity with deep learning-based denoising, *Geophys. J. Int.* ggae279.
- Deng, S., and A. Levander (2023). Seismic autocorrelation analysis of deep mars, *Geophys. Res. Lett.* **50**, e2023GL105046.
- Drilleau, M., H. Samuel, R. F. Garcia, A. Rivoldini, C. Perrin, C. Michaut, M. Wicczorek, B. Tauzin, J. A. D. Connolly, P. Meyer, *et al.* (2022). Marsquake locations and 1-d seismic models for mars from insight data, *J. Geophys. Res. Planets* **127**, no. 9, e2021JE007067.
- Durán, C., A. Khan, S. Ceylan, C. Charalambous, D. Kim, M. Drilleau, H. Samuel, and D. Giardini (2022). Observation of a core-diffracted *P*-wave from a farside impact with implications for the lower-mantle structure of Mars, *Geophys. Res. Lett.* **49**, no. 21, e2022GL100887.
- Durán, C., A. Khan, S. Ceylan, G. Zenhäusern, S. Stöhler, J. Clinton, and D. Giardini (2022). Seismology on Mars: An analysis of direct, reflected, and converted seismic body waves with implications for interior structure, *Phys. Earth Planet. Int.* **325**, 106851.
- Durán, C., A. Khan, J. Kemper, I. Fernandes, K. Mosegaard, J. Tromp, M. Dugué, D. Sollberger, and D. Giardini (2024). Searching the insight seismic data for mars’s background-free oscillations, *Seismol. Res. Lett.* doi: [10.1785/0220240167](https://doi.org/10.1785/0220240167).
- Helffrich, G. (2000). Topography of the transition zone discontinuities, *Rev. Geophys.* **38**, no. 1, 141–158.
- Huang, Q., N. C. Schmerr, S. D. King, D. Kim, A. Rivoldini, A.-C. Plesa, H. Samuel, R. R. Maguire, F. Karakostas, V. Lekić, *et al.* (2022). Seismic detection of a deep mantle discontinuity within Mars by InSight, *Proc. Natl. Acad. Sci.* **119**, no. 42, e2204474119.
- InSight Marsquake Service (2023). Mars seismic catalogue, insight mission; v14 2023-04-01, ETHZ, IPGP, JPL, ICL, Univ. Bristol, doi: [10.12686/a21](https://doi.org/10.12686/a21).
- Jacob, A., M. Plasman, C. Perrin, N. Fuji, P. Lognonné, Z. Xu, M. Drilleau, N. Brinkman, S. Stöhler, G. Sainton, *et al.* (2022). Seismic sources of InSight marsquakes and seismotectonic context of Elysium Planitia, Mars, *Tectonophysics* **837**, 229434.
- Kawamura, T., J. F. Clinton, G. Zenhäusern, S. Ceylan, A. C. Horleston, N. L. Dahmen, C. Duran, D. Kim, M. Plasman, S. C. Stöhler, *et al.* (2023). S1222a—the largest marsquake detected by insight, *Geophys. Res. Lett.* **50**, no. 5, e2022GL101543.
- Khan, A., S. Ceylan, M. van Driel, D. Giardini, P. Lognonné, H. Samuel, N. C. Schmerr, S. C. Stöhler, A. C. Duran, Q. Huang, *et al.* (2021). Upper mantle structure of Mars from InSight seismic data, *Science* **373**, no. 6553, 434–438.
- Khan, A., D. Huang, C. Durán, P. A. Sossi, D. Giardini, and M. Murakami (2023). Evidence for a liquid silicate layer atop the Martian core, *Nature* **622**, no. 7984, 718–723.
- Khan, D., C. Liebske, and J. A. D. Connolly (2021). An algorithm for thermodynamic parameter optimization: Application to the Martian mantle, *Geochem. Geophys. Geosyst.* **22**, no. 5, e2020GC009399.
- Lognonné, P., W. Banerdt, J. Clinton, R. Garcia, D. Giardini, B. Knapmeyer-Endrun, M. Panning, and W. Pike (2023). Mars seismology, *Annu. Rev. Earth Planet. Sci.* **51**, 643–670.
- Mittelholz, A., C. L. Johnson, S. N. Thorne, S. Joy, E. Barrett, M. O. Fillingim, F. Forget, B. Langlais, C. T. Russell, A. Spiga, *et al.* (2020). The origin of observed magnetic variability for a sol on mars from insight, *J. Geophys. Res. Planets* **125**, no. 9, e2020JE006505.
- Munch, F. D., A. Khan, B. Tauzin, A. Zunino, and D. Giardini (2018). Stochastic inversion of *P*-to-*S* converted waves for mantle composition and thermal structure: Methodology and application, *J. Geophys. Res.* **123**, no. 12, 10–706.

- Murphy, J. P., and S. D. King (2024). Reconciling mars insight results, geoid, and melt evolution with 3d spherical models of convection, *J. Geophys. Res. Planets* **129**, no. 5, e2023JE008143.
- Nissen-Meyer, T., M. van Driel, S. C. Stöhler, K. Hosseini, S. Hempel, L. Auer, A. Colombi, and A. Fournier (2014). AxiSEM: Broadband 3-D seismic wavefields in axisymmetric media, *Solid Earth* **5**, no. 1, 425–445.
- Posiolova, L. V., P. Lognonné, W. B. Banerdt, J. Clinton, G. S. Collins, T. Kawamura, S. Ceylan, I. J. Daubar, B. Fernando, M. Froment, *et al.* (2022). Largest recent impact craters on mars: Orbital imaging and surface seismic co-investigation, *Science* **378**, no. 6618, 412–417.
- Stähler, S. C., A. Mittelholz, C. Perrin, T. Kawamura, D. Kim, M. Knapmeyer, G. Zenhäusern, J. Clinton, D. Giardini, P. Lognonné, *et al.* (2022). Tectonics of Cerberus Fossae unveiled by marsquakes, *Nat. Astron.* **6**, 1376–1386.
- van Driel, M., S. Ceylan, J. F. Clinton, D. Giardini, A. Horleston, L. Margerin, S. C. Stöhler, M. Böse, C. Charalambous, T. Kawamura, *et al.* (2021). High-frequency seismic events on Mars observed by InSight, *J. Geophys. Res. Planets* **126**, no. 2, e2020JE006670.
- Zenhäusern, G., S. C. Stöhler, J. F. Clinton, D. Giardini, S. Ceylan, and R. F. Garcia (2022). Low-frequency Marsquakes and where to find them: Back azimuth determination using a polarization analysis approach, *Bull. Seismol. Soc. Am.* **112**, no. 4, 1787–1805.

---

Manuscript received 3 December 2024

Published online 3 June 2025